RSC Advances

Journal Name

ARTICLE

Rational synthesis of F-doped iron oxides on Al$_2$O$_3$(0001) single crystals

G. Carraro,[a] A. Gasparotto,*[a] C. Maccato,[a] E. Bontempi,[b] O. I. Lebedev,[c] C. Sada,[d] S. Turner,[e] G. Van Tendeloo[e] and D. Barreca[f]

A plasma enhanced-chemical vapor deposition (PE-CVD) route to Fe$_2$O$_3$-based materials on Al$_2$O$_3$(0001) single crystals at moderate growth temperatures (200-400°C) is reported. The use of the fluorinated Fe(hfa)$_2$TMEDA (hfa = 1,1,1,5,5,5-hexafluoro-2,4-pentanedionate; TMEDA = *N,N,N',N'*-tetramethylethylenediamine) molecular precursor in Ar/O$_2$ plasmas enabled an *in-situ* F-doping of iron oxide matrices, with a fluorine content tunable as a function of the adopted preparative conditions. Variations of the thermal energy supply enabled to control the system phase composition, resulting in the obtainment of γ-Fe$_2$O$_3$ at 200°C and of α-Fe$_2$O$_3$ nanostructures at higher deposition temperatures. Notably, at 400°C the formation of highly oriented α-Fe$_2$O$_3$ nanocolumns characterized by an epitaxial relation with the Al$_2$O$_3$(0001) substrate was observed. Beside fluorine content, phase composition and nano-organization, even the system optical properties and, in particular, energy gap values, could be tailored by proper modifications of processing parameters.

1 Introduction

In the last decades, iron(III) oxides have acquired a prominent role in various technological fields. For instance, α-Fe$_2$O$_3$ (*hematite*) has emerged as an outstanding electrode material for Graetzel cells and as an efficient catalyst/photocatalyst in various important reactions.[1-3] More recently, β- and ε-Fe$_2$O$_3$ have been reported to possess a catalytic activity even higher than *hematite* for solar hydrogen generation,[4] whereas γ-Fe$_2$O$_3$ (*maghemite*) is regarded as a promising magnetic material in particular for its superparamagnetic behavior.[1,5]

The extensive use of iron(III) oxides takes advantage not only of their non-toxicity, abundance and low cost, but also of the diversified properties of the various Fe$_2$O$_3$ polymorphs, providing such materials a strong potential for technological end-uses.[1,6-8] The functional behavior of Fe$_2$O$_3$ can be further tailored *via* chemical modification, for instance by the introduction of metallic nanoparticles or anionic doping,[9-11] the latter being much less explored. In particular, fluorine doping is the focus of an intense research interest, motivated by the possibility of tailoring iron oxide electrical, optical and chemical properties. For instance, F-doping can passivate defect states, enhance surface reactivity, and tune both electrical conductivity and light absorption properties.[9,12-20] Accordingly, fluorine doping candidates itself as a powerful tool to improve the system behavior in several applications encompassing photocatalysis, optoelectronics, energy storage and gas sensing.[8,15,18,19,21,22]

In addition, iron oxide properties can be tailored and optimized through a careful control of its nano-organization. For instance, in view of eventual photocatalytic/photoelectrochemical utilizations, columnar nanostructures join a high surface area with the possibility of absorbing a significant light fraction, while providing short carrier transport distances to the electrolyte.[9,23] Furthermore, the formation of heterojunctions at the interface with a single crystal substrate, or with a second nanostructured material, can suppress recombination processes, resulting in a higher quantum efficiency.[3,21]

On this basis, herein we report on the synthesis and chemico-physical characterization of F-doped iron oxides on Al$_2$O$_3$(0001) single crystals. As anticipated, fluorine doping and epitaxial growth play an important role from an applicative point of view, since they directly impact the material functional behavior. Nonetheless, fundamental understanding of structure/property interrelations, with particular regard to the role of doping and epitaxy on nucleation/growth phenomena, is still limited and represents a bottleneck for further research progresses. Specifically, F-doping of Fe$_2$O$_3$ or other metal oxides has been reported to influence crystallinity and, more specifically, to affect strain, grain size/shape and growth orientation.[7,15,17,19,21,22,24] On the other hand, the use of single crystal substrates can not only stabilize a specific polymorph, but also impact interface quality and surface faceting.[2,25-27]

In this work, F-doped iron oxides are synthesized by PE-CVD on Al$_2$O$_3$(0001) substrates starting from the fluorinated Fe(hfa)$_2$TMEDA molecular compound, that acts as *single-source* precursor for both Fe and F. Special attention was devoted to a detailed characterization of the system composition, morphology, nanostructure and optical properties by the complementary use of X-ray photoelectron spectroscopy (XPS), secondary ion mass spectrometry (SIMS), field emission-scanning electron microscopy (FE-SEM), bi-dimensional X-ray microdiffraction (XRD^2), (high resolution)-transmission electron microscopy [(HR)-TEM], electron diffraction (ED), and optical absorption measurements. The most relevant data are presented and critically discussed as a function of preparative conditions.

2 Experimental section

2.1 Synthesis

The Fe(hfa)$_2$TMEDA precursor was synthesized following a previously reported literature procedure.[28] Al$_2$O$_3$(0001) single crystals (10×10×1 mm^3, one-side polished) were purchased from Crystal GmbH (Berlin, Germany) and used as growth substrates without any further treatment. Deposition experiments were carried out using a two electrode radio frequency (RF; ν = 13.56 MHz) PE-CVD apparatus[29] in Ar/O$_2$ (gas flow rates = 15 and 20 sccm, respectively) plasmas. The total pressure, deposition time and RF power were kept constant at 1.0 mbar, 60 min and 10 W, respectively, using an interelectrode distance of 6.0 cm. Fe(hfa)$_2$TMEDA was vaporized at 65°C by means of an oil bath, and its vapors were transported into the reaction chamber by means of an Ar flow (rate = 60 sccm). The feeding gas lines were heated at 140°C to prevent precursor condensation phenomena. Under the above processing conditions, experiments were carried out at 200, 300 and 400°C to investigate the influence of growth temperature on the properties of the resulting iron oxide-based deposits.

2.2 Characterization

XPS analyses were performed on a Perkin-Elmer Φ 5600ci spectrometer, using a standard AlKα excitation source (1486.6 eV), at working pressures lower than 10^{-8} mbar. Binding energies (BEs, standard deviation = ±0.2 eV) were corrected for charging assigning a value of 284.8 eV to the adventitious C1s line.[30] Ar$^+$ sputtering was carried out at 3.0 kV (area = 2×2 mm^2, Ar partial pressure = 5×10^{-8} mbar). Atomic percentages (at. %) were calculated by signal integration using standard PHI V5.4A sensitivity factors. Peak fitting was performed by a least-squares procedure, adopting Gaussian-Lorentzian peak shapes.

SIMS analyses were carried out by means of an IMS 4f mass spectrometer (Cameca) using a 14.5 KeV Cs$^+$ primary beam (current = 25 nA, stability = 0.3%) and by negative secondary ion detection, adopting an electron gun for charge compensation. Beam blanking mode and high mass resolution configuration were adopted. Signals were recorded rastering over an area of 175×175 μm^2 and detecting secondary ions from a sub-region close to 8×8 μm^2 in order to avoid crater effects.

FE-SEM micrographs were collected by a Zeiss SUPRA 40VP instrument, with a primary beam voltage of 10 kV. The mean nanoaggregate size was evaluated through the SmartSEM® software by averaging over 20 independent measurements for each specimen.

XRD^2 images were collected by a Dymax-RAPID X-ray microdiffractometer with a cylindrical imaging plate detector, that allows collecting diffraction data in the ranges 2θ = 0 – 160° (horizontally) and 2θ = -45 – +45° (vertically) upon using CuKα radiation. The incident beam collimators enable different spot sizes to be projected onto the sample. In this work, measurements were performed in reflection mode, adopting a collimator diameter of 300 μm and an exposure time of 30 min for each XRD^2 pattern.

(HR)-TEM and ED experiments were carried out on a FEI Tecnai G2 30 UT microscope operated at 300 kV. High-angle annular dark-field STEM (HAADF-STEM) experiments were performed by an aberration-corrected Titan "cubed" microscope, operated at 300 kV. The used convergence semi-angle α and HAADF detector inner semi-angle β were 21 and 50 mrad, respectively. Specimens for cross-sectional (CS) and plane-view (PV) observations were prepared by mechanical polishing down to a thickness of approximately 20 μm, followed by Ar$^+$ ion milling under grazing angle down to electron transparency.

Optical absorption spectra were recorded by means of a Cary 5E (Varian) dual-beam spectrophotometer with a spectral bandwidth of 1 nm, operating in transmission mode at normal incidence. For each spectrum, the substrate contribution was subtracted. Optical band-gaps were estimated from Tauc plots (αhν)^2 vs. hν.[5,18,31]

3 Results and Discussion

3.1 Composition

In order to investigate the system surface and in-depth composition, XPS analyses were preliminarily carried out. Irrespective of the synthesis conditions, all samples were characterized by the presence of iron, oxygen, fluorine and carbon, the latter being limited to the outermost deposit layers. Fig. 1a displays the Fe2p surface peak for an iron oxide sample grown at 300°C. The Fe2p$_{3/2}$ signal was located at a BE of 711.0 eV with a spin-orbit separation of 13.5 eV. These data, along with the low intensity of *shake-up* satellites, are in good agreement with the presence of iron(III) oxide free from other Fe-containing species.[10,11,32-35] Accordingly, the main contribution to the O1s peak (see Fig. 1b, component **I**, 85.6% of the overall O signal) at 530.1 eV was attributed to lattice oxygen in Fe$_2$O$_3$.[26,32,35,36] The second band (component **II**) located at BE = 531.9 eV could be ascribed to adsorbed -OH groups and carbonates species arising from atmospheric exposure.[32,33]
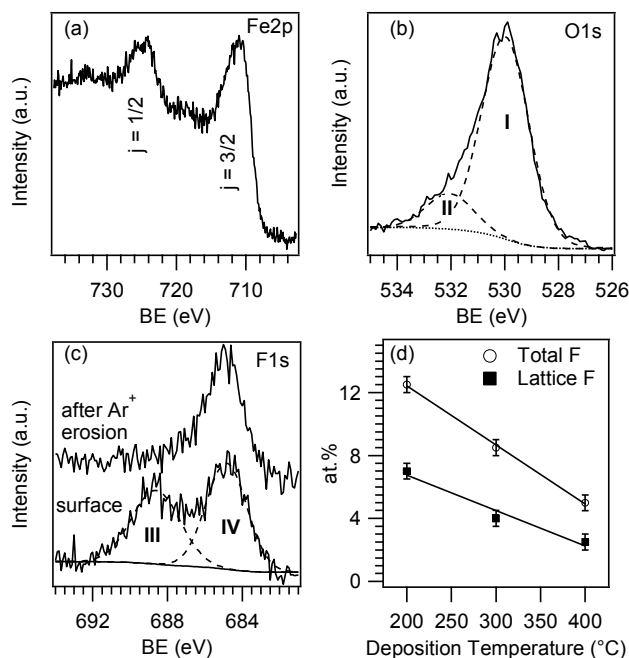

Fig. 1 Core-level photoelectron peaks for a specimen synthesized at 300°C: (a) Fe2p, (b) O1s, (c) F1s (before and after 5' Ar$^+$ sputtering). (d) Dependence of fluorine surface content on deposition temperature.

As can be observed, the F1s surface peak could be decomposed by means of two bands (Fig. 1c). Whereas the high BE one (component **III**, BE = 688.5 eV) was due to CF$_x$ species arising from an incomplete precursor decomposition,[10,33,37,38] component **IV** at 684.8 eV was traced back to F incorporation into iron oxide lattice,[7,10,32,38] indicating the formation of F-doped Fe$_2$O$_3$. Interestingly, the former signal disappeared upon a mild sputtering, highlighting that the presence of CF$_x$ moieties was limited to the outermost layers. Conversely, lattice fluorine was still clearly detectable after Ar$^+$ erosion (Fig. 1c). It is also worth noting that both the overall and lattice F surface content underwent a linear decrease upon increasing the deposition temperature (Fig. 1d), as already

observed under similar conditions.[9,39]

In order to investigate the fluorine distribution in the inner material layers, XPS and SIMS depth profiling were carried out (Fig. 2). Fig. 2a shows a representative XPS depth profile. The slight decrease of oxygen at. % occurring after the first 15 min of erosion is likely due to preferential sputtering phenomena, responsible also for the apparent increase of iron content.[30] Fluorine amount progressively decreased during the first erosion cycles and subsequently reached a constant value of *ca.* 2 at. % in the inner sample region. This behavior was related to the disappearance of surface CF_x species upon erosion, resulting in the presence of the sole lattice fluorine, that was homogeneously distributed in the iron oxide matrix.
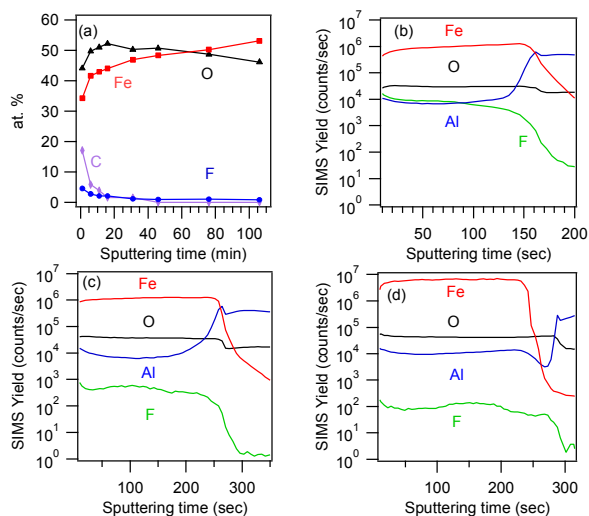

Fig. 2 (a) XPS depth profile for a sample deposited at 300°C. SIMS profiles for specimens grown at (b) 200°C, (c) 300°C and (d) 400°C.

The results of SIMS analyses (Figs. 2b-d) agreed to a good extent with XPS ones. In particular, irrespective of the adopted growth temperature, Fe, O and F ionic yield profiles were almost parallel throughout the entire nanodeposit thickness, indicating an uniform chemical composition and an even doping level. In addition, all samples showed a sharp and well defined interface with the substrate, allowing an accurate calculation of the deposit thickness. The pertaining values were 200±15, 260±15, and 170±15 nm at 200, 300 and 400°C, respectively.

3.2 Morphology

The influence of processing conditions on the system morphology was analyzed by FE-SEM (Fig. 3). At 200°C, plane-view investigation evidenced the formation of leaf-like lamellar nanostructures with an average lateral size and thickness of 80 and 25 nm, respectively. As evidenced by a closer micrograph inspection, such structures were composed by smaller and randomly oriented interconnected particles, suggesting the occurrence of a polycrystalline material.

Upon increasing the growth temperature to 300°C, the deposit morphology was only partially reminiscent of the previous one. In fact, the observed lamellar structures exhibited a more pronounced faceting and, in some cases, a well evident rectangular prism habit, with an in-plane size of 120 nm × 70 nm.

At 400°C, the system morphology underwent significant variations with respect to the previous cases. In fact, homogeneously distributed columnar structures aligned perpendicularly to the substrate surface could be observed. These nano-columns were characterized by displayed faceted tips, with average diameter and

length values of 30 and 170 nm, respectively. The obtainment of this nano-organization at the highest deposition temperature suggested a marked influence of the $Al_2O_3(0001)$ substrate on Fe_2O_3 nucleation and growth, as discussed in detail below.
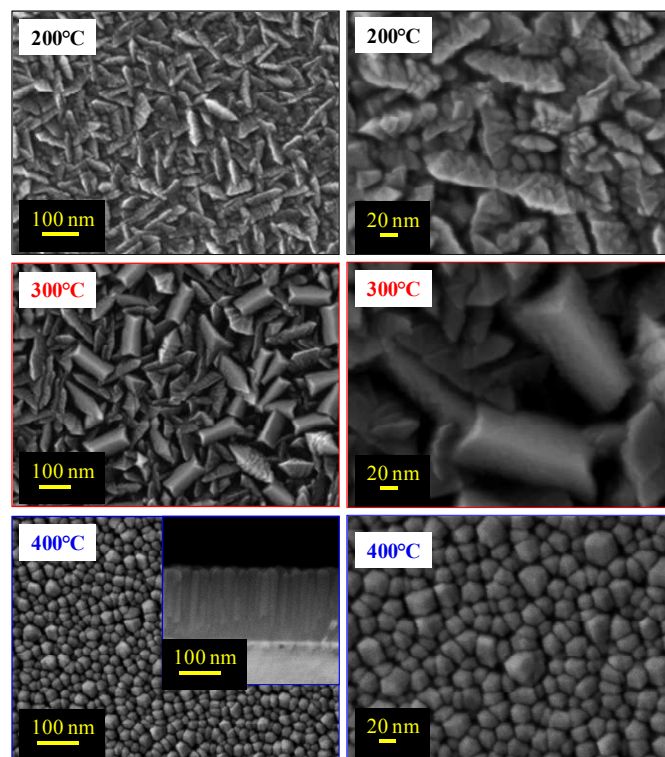

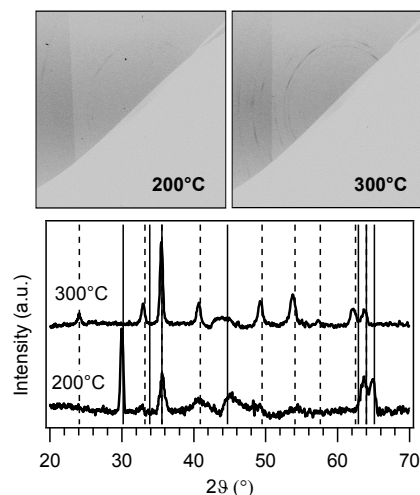**Fig. 3** FE-SEM PV micrographs of the iron oxide materials. The inset shows a cross-sectional image of the 400°C sample.

Fig. 4 XRD^2 maps and corresponding integrated spectra of specimens obtained at 200 and 300°C. Reflections expected for γ-Fe_2O_3[40] and α-Fe_2O_3[41] are marked by continuous and dashed lines, respectively.

3.3 Structure

The microstructural properties of the Fe_2O_3 nanomaterials were analyzed by two-dimensional X-ray diffraction and the pertaining XRD^2 maps are reported in Fig. 4, along with the corresponding integrated patterns. At the lowest deposition temperature (200°C), signals at 2ϑ = 30.0, 35.6, 63.7 and 65.0° were detected, and attributed to the (220), (311), (441) and (530) reflections of γ-Fe_2O_3

(*maghemite*).[40] On the other hand, the specimen deposited at 300°C displayed peaks at 24.1, 33.0, 35.5, 40.7, 49.2, 53.8, 57.3, 62.2, 63.6 and 74.9°, attributable to the (012), (104), (110), (113), (024), (116), (018), (214), (300) and (220) reflections of α-Fe$_2$O$_3$ (*hematite*).[41] In this case, a comparison with the powder reference spectrum indicated a preferred orientation along the <110> direction. The observed phase transition from *maghemite* (200°C) to *hematite* (300°C) was not surprising, and could be explained by the higher thermodynamic stability of α-Fe$_2$O$_3$.[1,6,34]

Nevertheless, at 400°C no reflections other than the substrate ones could be appreciated in the XRD^2 pattern (not reported). A similar finding suggests the occurrence of an epitaxial/oriented growth strongly affected by the underlying Al$_2$O$_3$(0001) support since, in a similar case, a full overlap between the substrate and the deposit

reflections is expected.[42]

In order to attain a deeper insight into this phenomenon, a detailed TEM analysis was carried out on the sample synthesized at 400°C. Low-magnification and high resolution PV and CS TEM images of the specimen, together with representative ED patterns taken from different sample areas, are displayed in Fig. 5.

PV observations indicated that individual grains had a *pseudo*-hexagonal morphology (see Fig. 5a), with typical diameters of nearly 40 nm. The PV HR-TEM image in Fig. 5b unambiguously confirmed the grain hexagonal structure, with predominantly exposed (-1010), (1-100) and (0-110) facets. Furthermore, CS data (Fig. 5c) evidenced an epitaxial, columnar, *c*-oriented *hematite* growth, with the following relationship: [0001] α-Fe$_2$O$_3$ // [0001] Al$_2$O$_3$ and (01-10) α-Fe$_2$O$_3$ // (01-10) Al$_2$O$_3$.
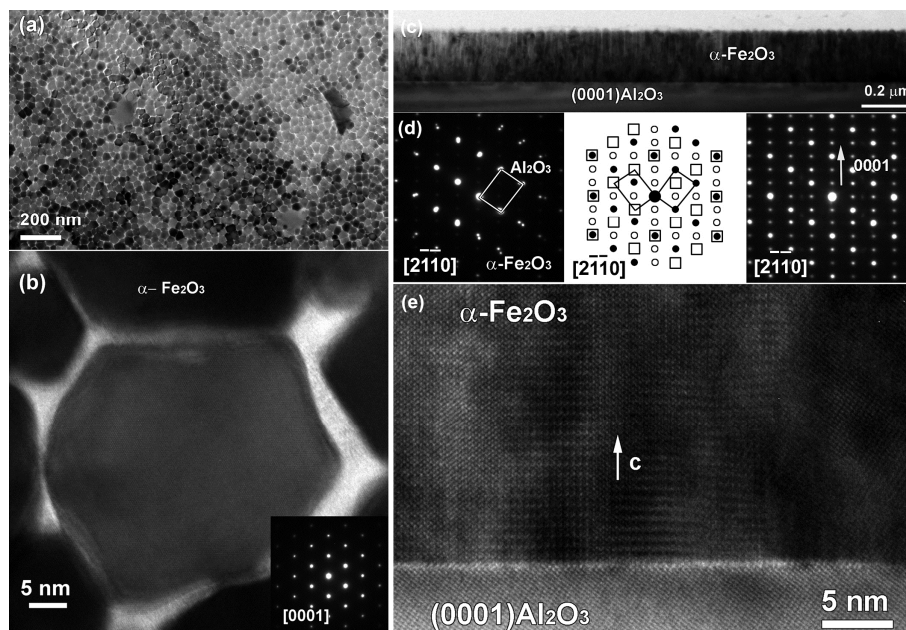

Fig. 5 (a) Low-magnification PV TEM image of the α-Fe$_2$O$_3$ sample deposited at 400°C. (b) PV HR-TEM image of the same specimen, with the corresponding ED pattern as inset. The grains are *c*-oriented and are imaged along the [0001] zone axis for α-Fe$_2$O$_3$. (c) Low-magnification CS TEM image of α-Fe$_2$O$_3$ on Al$_2$O$_3$ (0001). (d) Two selected CS ED patterns recorded in different areas, indicating the presence of *hematite* (left) and of a twinned structure (right). In the middle, a schematic drawing of the twinned structure, taking into account twinning over {01-10} type planes, combined with double diffraction, is presented. (e) HR-TEM image of a twinned α-Fe$_2$O$_3$ region.

The ED pattern in Fig. 5d left, imaged along the [2-1-10] zone axis orientation, is a superposition of the deposit and substrate structure, where the crystal phase of the former can be indexed using the space group and unit cell parameters of α-Fe$_2$O$_3$ [a = 0.503 nm, c = 1.374 nm, rhombohedral *R3-c*(167)].[2,35,43-45] Nevertheless, several ED images exhibited a more complex pattern, with various superstructure spots (compare Fig. 5d, right). A CS HR-TEM image taken from such a region is shown in Fig. 5e. The observed HR-TEM contrast and ED data can be likely traced back to the presence of regular twinnings within the α-Fe$_2$O$_3$ phase. A schematic view of the right-hand ED pattern, taking into account a twin structure over the (2-1-10) plane, is displayed in the central panel of Fig. 5d, where dots and squares correspond to two different α-Fe$_2$O$_3$ orientations sharing a common (0001) plane, whereas empty circles represent spots attributable to double diffraction phenomena.

PV and CS TEM data suggest *c*-oriented, randomly distributed grains with two different orientation variants A and B, related to each other by a 60° rotation along the [0001] axis. A model for such a kind of growth is presented in Fig. 6.

According to the proposed model, the difference between the two possibilities can be detected only in CS observations. Indeed, when the twin variants overlap, the structure observed in HR-TEM and ED patterns is expected to appear. Conversely, in the case of PV imaging, this rotation cannot be detected (see the top panel in Fig. 6).

In order to confirm the proposed twinned growth, HAADF–STEM imaging of the interface region was carried out. HAADF-STEM is mass-thickness sensitive, having image contrast that scales with the atomic number $Z^{~1.7}$. Since it is an incoherent imaging technique, diffraction contrast will not hinder the interpretation of the images, like in the case of HR-TEM. Fig. 7 shows representative high resolution HAADF-STEM images of a twinned area (Fig. 7a) and twin boundary (Fig. 7b). The structure models are overlaid, and match perfectly with the acquired images, confirming thus the validity of the proposed twinning model.
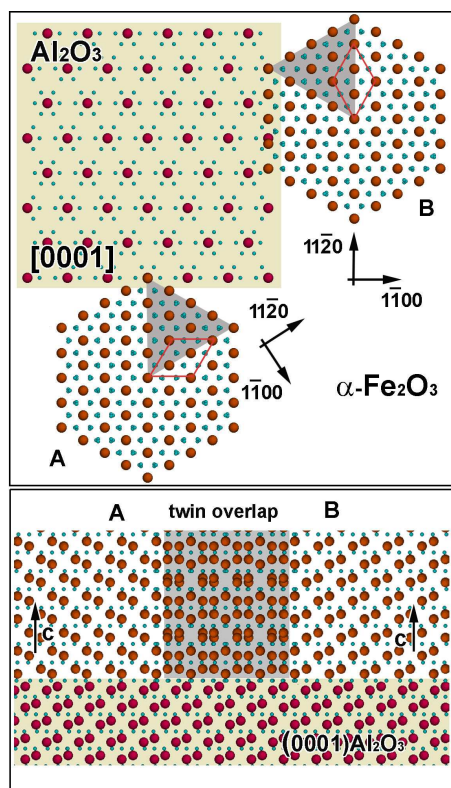
Fig. 6 Atomic model of α-Fe$_2$O$_3$, grown epitaxially on Al$_2$O$_3$ (0001), presented in two orthogonal view directions corresponding to PV (top) and CS (bottom) TEM observations.

Fig. 7 CS high resolution HAADF-STEM images along the [2-1-10] zone axis orientation of: (a) a twinned α-Fe$_2$O$_3$ region (A+B) next to a region of simple α-Fe$_2$O$_3$ (A); (b) a twin boundary in α-Fe$_2$O$_3$ (central arrow) showing the superstructure contrast in the boundary region.

3.5 Optical properties

Special attention was finally devoted to investigating the combined influence of F-doping and morphology/phase composition on the system optical properties, in order to better evaluate the suitability of the above materials for eventual optoelectronic or photocatalytic applications. In particular, as also reported for other metal oxides, oxygen replacement by fluorine can shift the absorption edge, affect the recombination between photogenerated electrons and holes, passivate defect states, and impact the system resistivity modifying carrier concentration and mobility.[9,11,12-16,19-21,38]

Fig. 8 displays the optical absorption spectra of iron oxide-based deposits grown at different temperatures. As can be observed, all specimens show a strong absorption for wavelengths lower than 600 nm, responsible for their red-to-yellow color.[46-48] Under the assumption of a direct allowed transition, the following band-gap values were derived from Tauc plots in Fig. 8: 2.52 eV, 2.22 eV and 2.16 eV for specimens grown at 200, 300 and 400°C, respectively. These values are significantly blue-shifted with respect to literature data for iron(III) oxides, that are typically close to 2.0 eV.[5,46,49] A similar finding suggests that, beside phase composition, even other parameters appreciably affect the system optical properties. More specifically, the obtainment of band-gap values appreciably higher than literature ones can be traced back to a modified carrier concentration in Fe$_2$O$_3$ conduction/valence bands when oxygen vacancies are saturated by fluorine.[9,19,20,50] This explanation also accounts for the progressive increase of band-gap values at the lowest deposition temperatures that, according to Figs. 1 and 2, result in a higher F-content in the obtained systems.
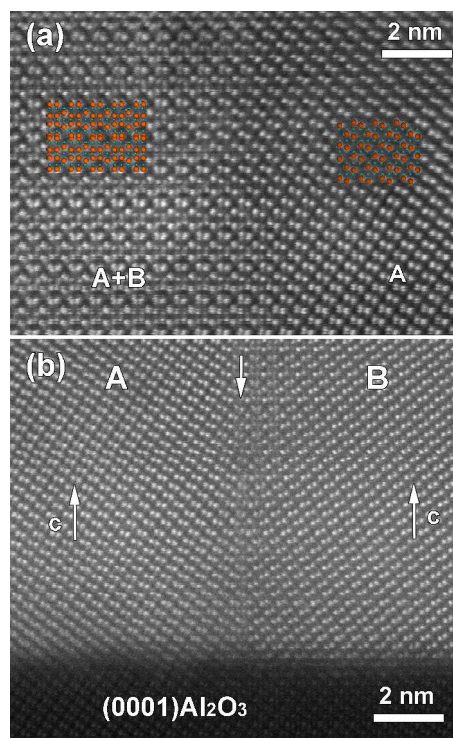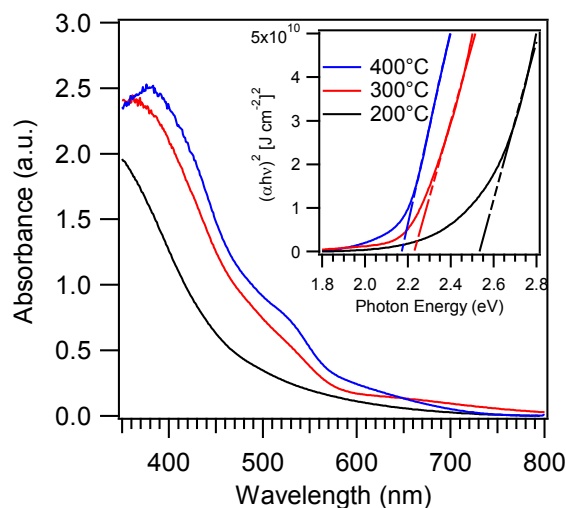

Fig. 8 Optical absorption spectra of iron oxide samples grown at 200, 300 and 400°C. The inset displays the corresponding Tauc plots.

Conclusions

A PE-CVD approach to Fe$_2$O$_3$-based nanostructures on Al$_2$O$_3$(0001) single crystal substrates has been reported. The obtained iron oxide nanomaterials were *in-situ* doped with fluorine thanks to the use of a fluorinated molecular compound, Fe(hfa)$_2$TMEDA, acting as a *single-source* precursor for both Fe and F. Controlled variations of the deposition temperature directly impacted both the system chemical composition and crystalline phase. In particular, a γ-Fe$_2$O$_3$ to α-Fe$_2$O$_3$ phase transition was observed upon going from 200 to

300°C, whereas highly oriented *hematite* nanocolumns were epitaxially grown at 400°C. A detailed structural and morphological investigation enabled to obtain a deep insight on the interrelations between processing parameters and composition, structure/morphology and optical properties of the target systems. The proposed fabrication process paves the way to the development of iron oxide nanosystems for various applications, in particular in the fields of optoelectronics and photocatalysis, for which control of fluorine content, nano-organization, and optical properties is expected to result in a parallel tuning of functional performances. Further developments of the current research will concern the influence of F-doping on the magnetic properties of Fe_2O_3. Following our recent paper on the magnetic behavior of β- and ε-Fe_2O_3,[51] future efforts will be specifically focused on the investigation of F-doped α- and γ-Fe_2O_3.

Acknowledgements

Notes and references

a Department of Chemistry, Padova University and INSTM, 35131 Padova, Italy.
b Chemistry for Technologies Laboratory, University of Brescia, 25123 Brescia, Italy.
c Laboratoire CRISMAT, UMR 6508, CNRS-ENSICAEN, 14050 Caen Cedex 4, France.
d Department of Physics and Astronomy, Padova University, 35131 Padova, Italy.
e EMAT, Antwerp University, 2020 Antwerpen, Belgium.
f IENI-CNR and INSTM, Department of Chemistry, Padova University, 35131 Padova, Italy.

1. L. Machala, J. Tuček and R. Zbořil, *Chem. Mater.*, 2011, **23**, 3255.
2. M. Lubbe, A. M. Gigler, R. W. Stark and W. Moritz, *Surf. Sci.*, 2010, **604**, 679.
3. D. Barreca, G. Carraro, A. Gasparotto, C. Maccato, F. Rossi, G. Salviati, M. Tallarida, C. Das, F. Fresno, D. Korte, U. Lavrenčič Štangar, M. Franko and D. Schmeisser, *ACS Appl. Mater. Interfaces*, 2013, **5**, 7130.
4. G. Carraro, C. Maccato, A. Gasparotto, T. Montini, S. Turner, O. I. Lebedev, V. Gombac, G. Adami, G. Van Tendeloo, D. Barreca and P. Fornasiero, *Adv. Funct. Mater.*, 2014, **24**, 372.
5. J. D. Desai, H. M. Pathan, S. K. Min, K. D. Jung and O. S. Joo, *Appl. Surf. Sci.*, 2006, **252**, 2251.
6. P. Tartaj, M. P. Morales, T. Gonzalez-Carreño, S. Veintemillas-Verdaguer and C. J. Serna, *Adv. Mater.*, 2011, **23**, 5243.
7. B. L. Lv, Z. Y. Liu, H. Tian, Y. Xu, D. Wu and Y. H. Sun, *Adv. Funct. Mater.*, 2010, **20**, 3987.
8. K. Karthikeyan, S. Amaresh, S. N. Lee, V. Aravindan and Y. S. Lee, *Chem. Asian J.*, 2014, **9**, 852.
9. D. Barreca, G. Carraro, A. Gasparotto, C. Maccato, C. Sada, A. P. Singh, S. Mathur, A. Mettenbörger, E. Bontempi and L. E. Depero, *Int. J. Hydrogen Energy*, 2013, **38**, 14189.
10. G. Carraro, D. Barreca, D. Bekermann, T. Montini, A. Gasparotto, V. Gombac, C. Maccato and P. Fornasiero, *J. Nanosci. Nanotechnol.*, 2013, **13**, 4962.
11. G. Carraro, D. Barreca, E. Comini, A. Gasparotto, C. Maccato, C. Sada and G. Sberveglieri, *CrystEngComm*, 2012, **14**, 6469.
12. H. Seo, L. R. Baker, A. Hervier, J. Kim, J. L. Whitten and G. A. Somorjai, *Nano Lett.*, 2011, **11**, 751.
13. A. Gasparotto, D. Barreca, D. Bekermann, A. Devi, R. A. Fischer, P. Fornasiero, V. Gombac, O. I. Lebedev, C. Maccato, T. Montini, G. Van Tendeloo and E. Tondello, *J. Am. Chem. Soc.*, 2011, **133**, 19362.
14. C. O'Keeffe, P. Gannon, P. Gilson, A. Kafizas, I. P. Parkin and R. Binions, *Thin Solid Films*, 2013, **537**, 131.
15. Y.-J., Choi and H.-H. Park, *J. Mater. Chem. C.*, 2014, **2**, 98.
16. A. Kafizas, N. Noor, P. Carmichael, D. O. Scanlon, C. J. Carmalt and I. P. Parkin, *Adv. Funct. Mater.*, 2014, **24**, 1758.
17. H. F. Liang and R. G. Gordon, *J. Mater. Sci.*, 2007, **42**, 6388.
18. I. Akyuz, S. Kose, E. Ketenci, V. Bilgin and F. Atay, *J. Alloys Compd.*, 2011, **509**, 1947.
19. J. Santos-Cruz, G. Torres-Delgado, R. Castanedo-Perez, C. I. Zuniga-Romero and O. Zelaya-Angel, *Thin Solid Films*, 2007, **515**, 5381.
20. R. Gonzalez-Hernandez, A. I. Martinez, C. Falcony, A. A. Lopez, M. I. Pech-Canul and H. M. Hdz-Garcia, *Mater. Lett.*, 2010, **64**, 1493.
21. C.-l. Song, J. Wang, M.-l. Zeng, J.-q. Zhu, Y. Liu, G. Xu and G.-r. Han, *J. Sol-Gel Sci. Technol.*, 2013, **68**, 121.
22. X. Noirfalise, T. Godfroid, G. Guisbiers and R. Snyders, *Acta Mater.*, 2011, **59**, 7521.
23. N. S. Chaudhari, S. S. Warule, S. Muduli, B. B. Kale, S. Jouen, B. Lefez, B. Hannoyer and S. B. Ogale, *Dalton Trans.*, 2011, **40**, 8003.
24. M. Kul, A. S. Aybek, E. Turan, M. Zor and S. Irmak, *Sol. Energy Mater. Sol. Cells*, 2007, **91**, 1927.
25. F. Bertram, C. Deiter, K. Pflaum, M. Suendorf, C. Otte and J. Wollschlager, *J. Appl. Phys.*, 2011, **110**, 102208.
26. T. Fujii, F. M. F. de Groot, G. A. Sawatzky, F. C. Voogt, T. Hibma and K. Okada, *Phys. Rev. B*, 1999, **59**, 3195.
27. S. Maheswaran, S. Thevuthasan, F. Gao, V. Shutthanandan, C. M. Wang and R. J. Smith, *Phys. Rev. B*, 2005, **72**, 7.
28. D. Barreca, G. Carraro, A. Devi, E. Fois, A. Gasparotto, R. Seraglia, C. Maccato, C. Sada, G. Tabacchi, E. Tondello, A. Venzo and M. Winter, *Dalton Trans.*, 2012, **41**, 149.
29. D. Barreca, A. Gasparotto, E. Tondello, C. Sada, S. Polizzi and A. Benedetti, *Chem. Vap. Deposition*, 2003, **9**, 199.
30. D. Briggs and M. P. Seah, *Practical Surface Analysis*, Wiley, New York, 1990.
31. N. A. M. Barakat, *J. Mater. Sci.*, 2012, **47**, 6237.
32. G. Carraro, A. Gasparotto, C. Maccato and D Barreca, *Surf. Sci. Spectra*, 2013, **20**, 9.
33. J. F. Moulder, W. F. Stickle, P. E. Sobol and K. D. Bomben, *Handbook of X-ray Photoelectron Spectroscopy*, Perkin Elmer Corporation, Eden Prairie, MN, USA, 1992.
34. P. Li, E. Y. Jiang and H. L. Bai, *J. Phys. D*, 2011, **44**, 075003.
35. S. I. Yi, Y. Liang, S. Thevuthasan and S. A. Chambers, *Surf. Science* 1999, **443**, 212.
36. Y. Gao, Y. J. Kim, S. A. Chambers and G. Bai, *J. Vac. Sci. Technol. A*, 1997, **15**, 332.
37. P. F. Fulvio, S. S. Brown, J. Adcock, R. T. Mayes, B. K. Guo, X. G.

Sun, S. M. Mahurin, G. M. Veith and S. Dai, *Chem. Mater.*, 2011, **23** 4420.

38. S. Sumitsawan, J. Cho, M. L. Sattler and R. B. Timmons, *Environ. Sci. Technol.*, 2011, **45**, 6970.

39. D. Barreca, D. Bekermann, E. Comini, A. Devi, R. A. Fischer, A. Gasparotto, M. Gavagnin, C. Maccato, C. Sada, G. Sberveglieri and E. Tondello, *Sens. Actuators B*, 2011, **160**, 79.

40. Pattern n°39-1346, JCPDS, 2000.

41. Pattern n°33-0664, JCPDS, 2000.

42. D. Barreca, A. Devi, R. A. Fischer, D. Bekermann, A. Gasparotto, M. Gavagnin, C. Maccato, E. Tondello, E. Bontempi, L. E. Depero and C. Sada, *CrystEngComm*, 2011, **13**, 3670.

43. A. Barbier, O. Bezencenet, C. Mocuta, J. B. Moussy, H. Magnan, N. Jedrecy, M. J. Guittet and M. Gautier-Soyer, *Mater. Sci. Eng. B*, 2007, **144**, 19.

44. C. M. Wang, S. Thevuthasan, F. Gao, D. E. McCready and S. A. Chambers, *Thin Solid Films*, 2002, **414**, 31.

45. I. J. Lee, J. Y. Kim, C. Yu, C. H. Chang, M. K. Joo, Y. P. Lee, T. B. Hur and H. K. Kim, *J. Vac. Sci. Technol., A*, 2005, **23**, 1450.

46. Y. P. He, Y. M. Miao, C. R. Li, S. Q. Wang, L. Cao, S. S. Xie, G. Z. Yang, B. S. Zou and C. Burda, *Phys. Rev. B*, 2005, **71**, 125411.

47. D. M. Sherman and T. D. Waite, *Am. Mineral.*, 1985, **70**, 1262.

48. D. A. Wheeler, G. M. Wang, Y. C. Ling, Y. Li and J. Z. Zhang, *Energy Environ. Sci.*, 2012, **5**, 6682.

49. B. Gilbert, J. E. Katz, J. D. Denlinger, Y. D. Yin, R. Falcone and G. A. Waychunas, *J. Phys. Chem. C*, 2010, **114**, 21994.

50. E. Burstein, *Phys. Rev.*, 1954, **93**, 632.

51. G. Carraro, D. Barreca, C. Maccato, E. Bontempi, L. E. Depero, César de Julián Fernández and A. Caneschi, *CrystEngComm*, 2013, **15**, 1039.